

See discussions, stats, and author profiles for this publication at: <https://www.researchgate.net/publication/221879548>

# Investigation of the Chemical Mixing State of Individual Asian Dust Particles by the Combined Use of Electron Probe X-ray Microanalysis and Raman Microspectrometry

ARTICLE *in* ANALYTICAL CHEMISTRY · MARCH 2012

Impact Factor: 5.64 · DOI: 10.1021/ac2029584 · Source: PubMed

---

CITATIONS

19

READS

30

## 8 AUTHORS, INCLUDING:



Sophie Sobanska

Université des Sciences et Technologies de Lille

108 PUBLICATIONS 795 CITATIONS

[SEE PROFILE](#)



Heejin Hwang

Korea Polar Research Institute

27 PUBLICATIONS 377 CITATIONS

[SEE PROFILE](#)



Hyo-Jin Eom

Inha University

20 PUBLICATIONS 81 CITATIONS

[SEE PROFILE](#)



Chul-Un Ro

Inha University

100 PUBLICATIONS 1,580 CITATIONS

[SEE PROFILE](#)

# Investigation of the Chemical Mixing State of Individual Asian Dust Particles by the Combined Use of Electron Probe X-ray Microanalysis and Raman Microspectrometry

Sophie Sobanska,<sup>†</sup> HeeJin Hwang,<sup>‡</sup> Marie Choël,<sup>†</sup> Hae-Jin Jung,<sup>§</sup> Hyo-Jin Eom,<sup>§</sup> HyeKyeong Kim,<sup>§</sup> Jacques Barbillat,<sup>†</sup> and Chul-Un Ro<sup>\*,§</sup>

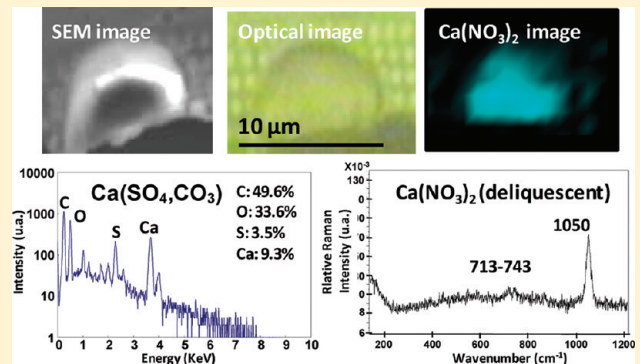
<sup>†</sup>Laboratoire de Spectrochimie Infrarouge et Raman, UMR CNRS 8516, Université de Lille 1, Bât. C5, 59655 Villeneuve d'Ascq Cedex, France

<sup>‡</sup>Korea Polar Research Institute, Songdo Dong, Yeonsu Gu, 406-840 Incheon, South Korea

<sup>§</sup>Department of Chemistry, Inha University, Yonghyun Dong, Nam Gu, 402-751 Incheon, South Korea

## Supporting Information

**ABSTRACT:** In this work, quantitative electron probe X-ray microanalysis (EPMA) and Raman microspectrometry (RMS) were applied in combination for the first time to characterize the complex internal structure and physicochemical properties of the same ensemble of Asian dust particles. The analytical methodology to obtain the chemical composition, mixing state, and spatial distribution of chemical species within single particles through the combined use of the two techniques is described. Asian dust aerosol particles collected in Incheon, Korea, during a moderate dust storm event were examined to assess the applicability of the methodology to resolve internal mixtures within single particles. Among 92 individual analyzed particles, EPMA and RMS identified 53% of the particles to be internally mixed with two or more chemical species. Information on the spatial distribution of chemical compounds within internally mixed individual particles can be useful for deciphering the particle aging mechanisms and sources. This study demonstrates that the characterization of individual particles, including chemical speciation and mixing state analysis, can be performed more in detail using EPMA and RMS in combination than with the two single-particle techniques alone.



**K**nowledge of the chemical composition, size, morphology, phase, and internal structure of single particles can provide insight into their physical, chemical, and optical properties. Over the past 40 years, some advanced microbeam analysis techniques have been used to provide spatially resolved information on the physical, morphological, and chemical properties of single particles formed in the atmosphere or in the laboratory.<sup>1–7</sup> Among them, energy-dispersive electron probe X-ray microanalysis (EPMA) based on a scanning electron microscope (SEM) equipped with an ultrathin energy-dispersive X-ray (EDX) detector provides information on the size and elemental compositions of individual particles with submicrometer lateral resolution.<sup>1,5</sup> Computer-controlled SEM/EDX can provide quantitative information on the elemental composition of a large number of particles<sup>8–11</sup> and has been used successfully to characterize a range of atmospheric aerosol samples.<sup>12–21</sup> Although very powerful, EPMA has limited capabilities for performing molecular speciation of particles and probing semivolatile particles under nondestructive conditions due to the electron beam used and/or high vacuum maintained in the sample chamber. Alternatively, vibrational spectroscopic techniques are powerful

for functional group analysis and molecular speciation of organic and inorganic chemical compounds including hydrated species under ambient conditions. Thus far, studies of the molecular characterization and/or hygroscopic properties of size-segregated aerosol particle samples are often performed using Fourier transform infrared (FT-IR) spectroscopy<sup>22–28</sup> or confocal Raman microspectrometry (RMS).<sup>29–31</sup>

Recently, the combined application of EPMA and vibrational microspectrometric techniques for the characterization of heterogeneous individual particle ensembles was reported.<sup>32–42</sup>

In particular, the combination of RMS and EPMA can provide unambiguous chemical and structural information on heterogeneous environmental particles with a spatial resolution of <1 μm.<sup>2,32–34,36,40–42</sup> On the other hand, in previous studies, only Raman point analysis was performed without the systematic elemental quantification obtainable by EPMA and/or RMS and EPMA were applied separately for aerosol samples (not on the same individual particles), in which the chemical

Received: November 8, 2011

Accepted: March 1, 2012

Published: March 1, 2012



complexity of airborne particles cannot be fully described. Although the combined application of FT-IR microimaging and quantitative EPMA techniques for the characterization of the same individual airborne particles (but at different spatial resolutions) has recently been published,<sup>35,37–39</sup> the combined application of Raman imaging and quantitative EPMA techniques has never been performed on the same particles. In the present study, airborne particles collected during an Asian dust storm event were investigated by the combined use of EPMA and RMS to demonstrate the potential of the combined use of the two single-particle analytical techniques on the same individual particles. EPMA provides information on the morphology and elemental concentrations, and RMS gives information on the molecular species and chemical mixing states.

Asian dust storms inject immense quantities of dust particles from arid and semiarid areas into the atmosphere and periodically contribute to the large global aerosol load.<sup>43–45</sup> These particles can be transported to eastern parts of Asia over long distances and affect the radiative balance,<sup>46</sup> prevalence of ice nuclei and cloud condensation nuclei,<sup>47,48</sup> and the atmospheric deposition of nutrients and toxins.<sup>49,50</sup> Mineral dust particles provide reactive surfaces for heterogeneous reactions with trace atmospheric gases, leading to chemical modification of the particles that ultimately affects the atmospheric chemical balance and photochemical cycle.<sup>51,52</sup> At the same time, modification of the physicochemical properties of particles can alter their optical properties as well as their direct and indirect radiative forcings.<sup>53,54</sup> Therefore, increasing attention has been devoted to studies of the atmospheric processing of Asian mineral dust during long-range transport.<sup>55–59</sup> In this work, quantitative EPMA and Raman imaging techniques were applied in combination for the first time to characterize the complex internal structure and physicochemical properties of the same ensemble of Asian dust particles.

## EXPERIMENTAL SECTION

**Samples.** The samples were collected from the rooftop of a campus building in Inha University (approximately 20 m above ground level), which is located in Incheon, Korea ( $37.45^{\circ}$  N,  $126.73^{\circ}$  E) near the west coast of the Korean peninsula. Normally during spring, Asian dust storm events occur over the Korean peninsula. According to the meteorological data provided by the Korea Meteorological Administration, the monthly average concentration of particles  $<10\text{ }\mu\text{m}$  in aerodynamic diameter ( $\text{PM}_{10}$ ) in Incheon is approximately  $80\text{ }\mu\text{g m}^{-3}$  over the spring period. Severe dust events with a concentration of  $\text{PM}_{10}$  reaching  $1000\text{ }\mu\text{g m}^{-3}$  can occur sporadically. During such events, mineral dust has been reported to be mixed with anthropogenic pollutants, resulting in a physicochemical transformation of these particles.<sup>20,60–63</sup> Three samples (S1–S3) were collected on March 27–29, 2007. Although sample S2 was collected during a moderate dust storm event with a mean  $\text{PM}_{10}$  concentration of  $\sim 210\text{ }\mu\text{g m}^{-3}$ , samples S1 and S3 were collected at the beginning and end of the dust storm event with mean  $\text{PM}_{10}$  concentrations of  $\sim 95$  and  $\sim 40\text{ }\mu\text{g m}^{-3}$ , respectively. The particles were collected using a three-stage cascade impactor (Dekati PM-10 sampler, Dekati Ltd.). At a flow rate of  $10\text{ L min}^{-1}$ , the aerodynamic diameter ranges for stages 1–3 were  $>10$ , 2.5–10, and 1.0–2.5  $\mu\text{m}$ , respectively. The particles collected on stages 2 (called the “coarse” fraction for convenience) and 3 (called the “fine”

fraction for convenience) were analyzed. The particles were deposited on transmission electron microscopy (TEM) grids (Ted Pella Inc., Redding, CA; Formvar/carbon 200 mesh Ni grid, 30–50 nm thickness). According to a previous study,<sup>64</sup> the choice of optimal substrate material for particle collection is critical for the successful application of both EPMA and RMS. A substrate with a flat surface is appropriate as the topography (surface roughness) is an important parameter for the good visual recognition of particles on secondary electron and optical images. TEM grids have a low Bremsstrahlung background for EPMA measurements<sup>65</sup> and are suitable for RMS measurements due to their flat stable surface (strong enough not to move due to heat transfer), lack of a strong Raman signal from the substrate (or a low reproducible background), and tolerance for laser power. The Raman signals from the amorphous carbon film of TEM grids were observed as two broad Raman bands at  $1300$  and  $1600\text{ cm}^{-1}$ , which were assigned to the D and G bands, respectively.<sup>66</sup> However, the ultrathin carbon film (3–4 nm) provides sufficiently low Raman signals that can be subtracted easily from that of coarse carbonaceous particles.<sup>32</sup>

**RMS and Raman Imaging Measurements.** TEM grids with the particles were placed on the microscope stage of a confocal Raman microspectrometer (LabRAM, Horiba Jobin-Yvon) equipped with a  $100\times$ , 0.9 numerical aperture objective (Olympus). Raman scattering was performed at a wavelength of  $632.8\text{ nm}$  with a He–Ne laser and detected with a  $\text{N}_2$ -cooled charge-coupled device (CCD) detector. The laser power delivered to the sample was approximately  $8\text{ mW}$  and could be attenuated by a set of neutral density filters with an optical density ranging from 0.3 to 4. The spot size of the laser at the sample was estimated to be  $\sim 1\text{ }\mu\text{m}^2$ . A confocal hole,  $350\text{ }\mu\text{m}$  in diameter, was used, giving an axial resolution ( $Z$ ) of approximately  $3.4\text{ }\mu\text{m}$ . The spectra were acquired using LabSpec software. For each analysis, two spectral ranges, i.e.,  $150$ – $1250$  and  $1000$ – $2000\text{ cm}^{-1}$ , were explored. The XYZ computer-controlled Raman mapping was performed by obtaining the Raman spectra in a point-by-point XY scanning mode ( $y$  rows,  $x$  points per row) with a  $1\text{ }\mu\text{m}$  step, 10 s integration time, and one accumulation, which was carried out at ambient relative humidity ( $\text{RH} = \sim 60\%$ ). The absence of laser damage to the sample was verified by comparing the optical images recorded before and after Raman mapping. The Raman mapping generates a three-dimensional data set ( $x \times y \times \lambda$ ), i.e.,  $x \times y$  spectra, each containing  $\lambda = 2040$  spectral elements corresponding to a spectral range of approximately  $1000\text{ cm}^{-1}$  with a spectral resolution of  $4\text{ cm}^{-1}$ . From this data set, the pure Raman spectrum including the polarized spectrum and spatial distribution of each species were obtained with a powerful multivariate curve resolution (MCR) data treatment (SIMPLISMAX),<sup>32,67</sup> which is briefly described in the Supporting Information.

**EPMA Measurements.** The measurements were carried out on a Jeol JSM-6390 SEM equipped with an Oxford Link SATW ultrathin window EDX detector allowing the detection of low-Z elements, such as C, N, and O. The spectral resolution of the detector was  $133\text{ eV}$  for  $\text{Mn K}\alpha$  X-rays. The X-ray spectra were recorded using INCA software (Oxford). An accelerating voltage of  $10\text{ kV}$ , a beam current of  $0.5\text{ nA}$ , and a typical measuring time of  $15\text{ s}$  were employed to ensure a low background level for the spectra, good sensitivity for low-Z element analysis, and statistically significant characteristic X-ray counts. More details on the EPMA measurements are reported

elsewhere.<sup>11</sup> The net X-ray intensities for chemical elements were obtained by nonlinear, least-squares fitting of the collected spectra using the AXIL program.<sup>68</sup> The elemental concentrations of individual particles were determined from their X-ray intensities using a Monte Carlo calculation combined with reverse successive approximations.<sup>10</sup> The quantitative procedure based on the Monte Carlo simulation provided results accurate to within 12% relative deviations between the calculated and nominal elemental concentrations for the various standard particles.<sup>8,10,69</sup> By the use of the “expert system” program,<sup>9</sup> individual particles were classified into different particle types on the basis of their chemical compositions and morphologies. The basic classification rules are given elsewhere.<sup>63</sup>

**Combined Use of EPMA and RMS.** RMS allows the molecular characterization of particles under ambient conditions, whereas EPMA measurements are performed under high vacuum ( $7 \times 10^{-4}$  Pa), possibly causing the dehydration of liquid or deliquescent particles. Therefore, Raman measurements for the individual Asian dust particles were first carried out, and the X-ray spectra of the same individual particles examined previously by RMS were acquired after the particles were relocated using secondary electron and optical images recorded with the same magnification in a manner similar to that described previously.<sup>35</sup> The molecular species determined from the pure Raman spectra were checked for consistency with the elemental compositional data obtained by EPMA. As a single particle can contain several chemical species, resulting from atmospheric coagulation, aggregation, or chemical reaction of the particles, the mixing state of the internal mixture particle can be described better by the Raman images of each molecular species within the particle.

## ■ RESULTS AND DISCUSSION

**Elemental and Molecular Characterization of the Individual Asian Dust Particles.** Among the 92 particles analyzed in samples S1–S3 using RMS and EPMA, four particle groups were encountered: primary soil-derived particles (62%), reacted soil-derived particles (7%), reacted sea-salt particles (9%), and sea salt mixed with soil-derived particles (22%). A unique notation was devised for the specific particle types determined by EPMA; e.g., C–SiO<sub>2</sub>–Fe<sub>2</sub>O<sub>3</sub> indicates that carbonaceous, SiO<sub>2</sub>, and Fe<sub>2</sub>O<sub>3</sub> species are the major components (>10%), and (Ca,Mg)(NO<sub>3</sub>,SO<sub>4</sub>) indicates that the particle is composed of an internal mixture of Ca(NO<sub>3</sub>)<sub>2</sub>, CaSO<sub>4</sub>, Mg(NO<sub>3</sub>)<sub>2</sub>, and MgSO<sub>4</sub>. Tables S1 and S2 of the Supporting Information provide a detailed description of the particle types, including their mean elemental concentrations obtained by X-ray analysis and their corresponding molecular identification.

**Primary Soil-Derived Particles.** Asian dust particles of a soil origin mostly contain mineral particles, such as silicates, oxides, and carbonates.<sup>20,60–63,70</sup> Chemical elements such as Si, Al, Na, K, Ca, Mg, and/or Fe are the common constituents of soil-derived airborne mineral dust particles. On the basis of the EPMA measurements, soil-derived particle groups were differentiated into carbonates, oxides, calcium sulfate, and silicates (Table S1, Supporting Information). Primary soil-derived particles account for 26%, 72%, and 77% of the S1, S2, and S3 samples, respectively, which shows that Asian dust particles are of soil origin.

Carbonates are abundant in northern Chinese crustal materials,<sup>20,60–63</sup> and the carbonate-containing particles iden-

tified by EPMA in samples S1–S3 included C–CaCO<sub>3</sub>, (Ca,Na,Mg)CO<sub>3</sub>, and (Ca,Na,Mg,K)CO<sub>3</sub>. The presence of calcite (CaCO<sub>3</sub>) and dolomite (CaMg(CO<sub>3</sub>)<sub>2</sub>) in the particles assigned to CaCO<sub>3</sub> and (Ca,Mg)CO<sub>3</sub> particle types was confirmed by their intense Raman bands at 1086 and 1097 cm<sup>-1</sup>, respectively, which are symmetric stretching vibrations ( $\nu_1$ ) of CO<sub>3</sub><sup>2-</sup> in calcite and dolomite structures.<sup>71</sup> Regarding (Ca,Na,Mg)CO<sub>3</sub> and (Ca,Na,Mg,K)CO<sub>3</sub> particle types by EPMA, Raman analysis clearly indicated the presence of calcite and dolomite, respectively. The partial substitution of Ca and/or Mg with K and/or Na in the calcite or dolomite structures does not affect the Raman band positions observed for the defined compounds.

Oxides classified by EPMA included SiO<sub>2</sub>, SiO<sub>2</sub>–C, and FeO<sub>x</sub>–C–SiO<sub>2</sub> particle types. In the same particles, RMS identified SiO<sub>2</sub> species as quartz ( $\alpha$ -SiO<sub>2</sub>) with a characteristic Raman band at 464 cm<sup>-1</sup> and iron oxide species as hematite ( $\alpha$ -Fe<sub>2</sub>O<sub>3</sub>) with the main Raman bands at 224, 245, 296, 410, 500, 610, and 659 cm<sup>-1</sup>. A typical example of an individual SiO<sub>2</sub> particle (particle A in Figure S1 of the Supporting Information) was composed of O (65.0%) and Si (33.0%) and confirmed as quartz ( $\alpha$ -SiO<sub>2</sub>) by RMS. The carbonaceous species detected by X-ray analysis was not identified by RMS. Since carbonaceous species such as graphite and soot have a large Raman cross-section, they might contain organic carbon from a soil origin, such as humic or humic-like substances.

Calcium sulfate particles are often encountered in Asian dust samples.<sup>18</sup> EPMA identified the C–CaSO<sub>4</sub> particle type only in sample S3 (Table S1, Supporting Information), where 9 of 40 particles analyzed were CaSO<sub>4</sub>-containing particles. RMS clearly identified their mineral type as gypsum (CaSO<sub>4</sub>·2H<sub>2</sub>O) due to its characteristic  $\nu_1$ (SO<sub>4</sub><sup>2-</sup>) vibration band at 1008 cm<sup>-1</sup> (Table S2, Supporting Information), which belongs to a primary soil-derived particle type.

The soil-derived particles encountered most frequently were aluminosilicates (denoted as AlSi in EPMA analysis), in which O, Si, and Al are the major elements, with minor contributions from C, Na, Mg, K, Ca, Ti, and/or Fe. According to EPMA, many different particle types were observed in the “soil-derived” particle group, including AlSi(C,K), AlSi(C,Na), AlSi(C,K,Ca), AlSi(C,Mg,K), AlSi(C,Na,Mg), AlSi(C,Mg,K,Fe), AlSi(C,Mg,K,Ca), and AlSi(Mg,K,Ti,Fe), where chemical elements listed in parentheses are minor ones (<5 atom %) (Table S1, Supporting Information). Some AlSi(C,Na)- and AlSi(C,K)-type particles were identified by RMS as feldspar minerals, such as Na-feldspar (NaAlSi<sub>3</sub>O<sub>8</sub>) and K-feldspar (KAlSi<sub>3</sub>O<sub>8</sub>), respectively. The mean elemental compositions determined by EPMA of AlSi(C,Na)- and AlSi(C,K)-type particles were 61.3 atom % O, 23.8 atom % Si, 9 atom % Al, and 5 atom % Na and 56.4 atom % O, 24.8 atom % Si, 8.4 atom % Al, and 5.8 atom % K, respectively, which matched the stoichiometry of Na- and K-feldspars well.

Most of the aluminosilicate particles identified by EPMA contained carbonaceous species (denoted as “C” in particle-type representation), most possibly humic substances due to their soil origin.<sup>72</sup> The RMS spectra of those aluminosilicate particles showed a strong fluorescence signal, probably due to the humic substances intercalated between sheets of swelling clay minerals. The MCR data treatment can resolve the fluorescence signals from the background and fluorescent clay minerals as two separate Raman spectra,<sup>67</sup> and the latter spectrum can be used as indirect proof of clay minerals. According to RMS, many aluminosilicate particles were

identified just as clay minerals as their Raman spectra showed a strong fluorescent signal without the Raman bands characteristic of specific silicate minerals. For example, particle B shown in Figure 1 belongs to the AlSi(C,Na,Mg) particle type. The

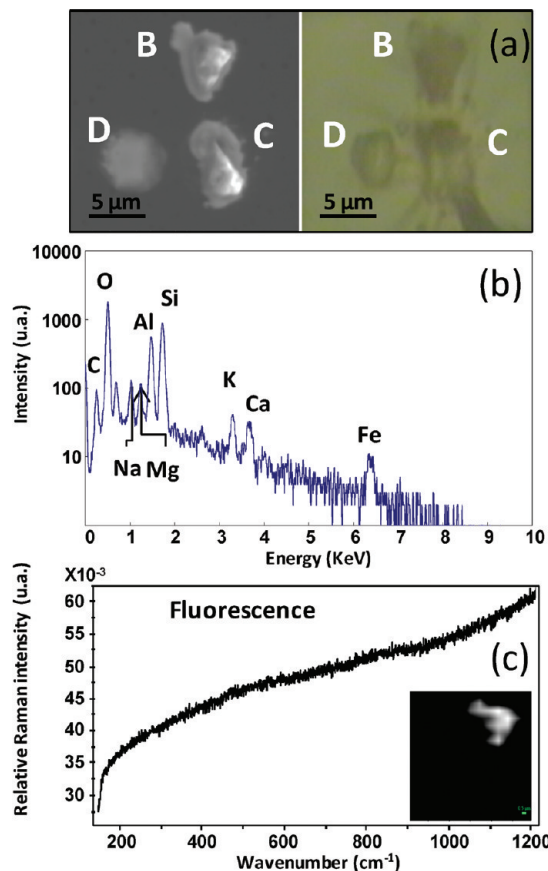


**Figure 1.** Elemental and molecular compositions of the clay mineral particles: (a) SEM and optical images showing particles B–D; (b) X-ray spectrum of particle B; (c) Raman spectrum and corresponding Raman image (after smoothing procedure) of particle B.

elemental composition and particle assignment were deduced from the X-ray spectrum (Figure 1b) acquired by EPMA as described in the Experimental section. The Raman spectrum resolved from the Raman mapping data exhibited a strong fluorescent signal (see Figure 1c and Figure S2 of the Supporting Information for the other examples). The reconstructed Raman image for the fluorescent signal (inset in Figure 1c) matched both the SEM and optical images of particle B well, demonstrating that the fluorescence signals from the particles and collecting substrate can be resolved. Thus, the fluorescent spectrum and corresponding image can be used as indirect proof of clay mineral particles. The reconstructed Raman image was obtained by the application of the MCR procedure.<sup>67</sup> The MCR procedure allows extraction of some pure Raman spectra (meaning one spectrum for one species) from the whole spectral data set and estimating the quantitative contribution of each pure spectrum in each pixel of the image. The MCR procedure also allows the reconstruction of the Raman image by linear combination of pure Raman spectra weighted by their contribution on each pixel of the image. A description of the MCR procedure for reconstructing the Raman image can be found in the Supporting Information.

Some particles exist as mixtures of silicates and other soil-derived species, such as  $\text{CaCO}_3$ ,  $\text{Fe}_2\text{O}_3$ , and  $\text{SiO}_2$ , as discussed in previous studies.<sup>73</sup> The particle types determined by EPMA were  $\text{FeO}_x-\text{C}-\text{SiO}_2$ ,  $\text{CaCO}_3-\text{AlSi}$ ,  $\text{CaCO}_3-\text{AlSi}(\text{Mg},\text{K},\text{Ca})$ ,  $(\text{Ca},\text{Mg})\text{CO}_3-\text{AlSi}$ ,  $(\text{Na},\text{Ca})\text{CO}_3-\text{C}-\text{AlSi}(\text{Mg})$ ,  $\text{AlSi}-(\text{Ca},\text{Mg},\text{Fe})\text{CO}_3$ ,  $\text{AlSi}-(\text{Ca},\text{Mg},\text{K},\text{Fe})\text{CO}_3$ ,  $\text{AlSi}-\text{Fe}_2\text{O}_3-(\text{C},\text{Mg},\text{Ti})$ , and  $\text{CaCO}_3-\text{SiO}_2-\text{C}$ . These particle types accounted for 24% of the primary soil-derived particles in samples S1–S3. Indeed, RMS analysis of these particles confirmed that they were mixtures of pure species. For example, a  $\text{CaCO}_3-\text{SiO}_2-\text{C}$  particle with an elemental composition of 23.6% C, 59.7% O, 2.4% Si, and 11.7% Ca by EPMA was identified by RMS to be a mixture of quartz and calcite. Nevertheless, it is not rare to observe only a strong fluorescent signal from clay minerals, obscuring the Raman signal from the specific silicate minerals.

**Reacted Soil-Derived Particles.** Nitric and sulfuric acids formed by the oxidation of  $\text{NO}_x$  and  $\text{SO}_x$  in the atmosphere can be totally or partially neutralized by alkaline species in dust particles to produce sulfate or nitrate species.<sup>74</sup> These dust particles are referred to as secondary or reacted ones. The common type of reacted soil-derived particles was “reacted  $\text{CaCO}_3$ ”, which contained  $\text{Ca}(\text{NO}_3)_2$  and/or  $\text{CaSO}_4$  as the reaction products of  $\text{CaCO}_3$  with nitrogen and/or sulfur oxide species, respectively.<sup>75,76</sup> EPMA identified  $\text{Ca}(\text{CO}_3,\text{SO}_4)-\text{C}$ ,  $\text{C}-\text{Ca}(\text{SO}_4,\text{NO}_3)$ ,  $\text{C}-\text{AlSi}-\text{Fe}_2\text{O}_3-\text{NO}_3$ , and  $\text{C}-\text{AlSi}(\text{K},\text{NO}_3)$  particle types. RMS showed that the reacted soil-derived particles were internal mixtures of chemical species, such as  $\text{CaCO}_3$ ,  $\text{Ca}(\text{NO}_3)_2$ ,  $\text{CaSO}_4$ , and/or clay minerals. Deliquescent  $\text{Ca}(\text{NO}_3)_2$  aerosol particles were expected to be in an ambient atmosphere because  $\text{Ca}(\text{NO}_3)_2$  particles are in an aqueous phase above 11% relative humidity.<sup>77</sup> This was confirmed by RMS, as this technique can distinguish deliquescent and crystalline  $\text{Ca}(\text{NO}_3)_2$  species according to their distinct  $\nu_1$  Raman bands at 1053 and 1066  $\text{cm}^{-1}$ , respectively. Anhydrite (anhydrous  $\text{CaSO}_4$ ) was observed as a reaction product of  $\text{CaCO}_3$  with sulfur oxide species. Gypsum and anhydrite can be differentiated easily by RMS using their characteristic Raman bands at 1008 and 1015  $\text{cm}^{-1}$  ( $\text{SO}_4^{2-}$  symmetric stretching mode), respectively (Table S2, Supporting Information).

**Reacted Sea-Salt Particles.** Marine-originated aerosols are frequently encountered in samples collected in Incheon due to its coastal location.<sup>18</sup> Genuine sea-salt aerosols can react with nitrogen and sulfur oxide species in the atmosphere to form “aged” sea salts, normally composed of  $\text{NaNO}_3$  and/or  $\text{NaSO}_4$ , resulting in chlorine depletion.<sup>18,63,72</sup> EPMA revealed the “reacted sea-salts” group to be comprised of  $(\text{Na},\text{Mg})(\text{NO}_3,\text{Cl})$ ,  $(\text{Na},\text{Mg})(\text{NO}_3,\text{SO}_4)$ , and  $(\text{Na},\text{Mg})(\text{NO}_3,\text{SO}_4,\text{Cl})$  particle types. Some particles contained a small amount of Cl, showing the incomplete transformation of genuine sea-salt particles. The selection rules of Raman scattering indicate no fundamental Raman active modes for chlorine salts, such as  $\text{NaCl}$ ,  $\text{KCl}$ ,  $\text{MgCl}_2$ , and  $\text{CaCl}_2$ , so that chlorine salt species cannot be identified by Raman spectroscopy. RMS analysis of the reacted sea-salt particles confirmed the presence of  $\text{Na}_2\text{SO}_4$  in phase V (stable at room temperature) ( $\nu_1(\text{SO}_4^{2-}) = 992 \text{ cm}^{-1}$ ) and solid  $\text{NaNO}_3$  for sulfate and nitrate species determined by EPMA, respectively. Although Mg was detected by EPMA within the particles,  $\text{MgSO}_4 \cdot x\text{H}_2\text{O}$  (with  $x = 4-7$ ) compounds were not identified by RMS due to the lack of characteristic Raman bands at 984 or 998  $\text{cm}^{-1}$ . On the other hand, an evaporated compound, such as bloedite ( $\text{Na}_2\text{Mg}(\text{SO}_4)_2 \cdot 4\text{H}_2\text{O}$ ), was identified from its typical Raman bands at 460, 637, and

996 cm<sup>-1</sup>. Although Na<sub>2</sub>SO<sub>4</sub> in phase III, which has an intense Raman band at 996 cm<sup>-1</sup>, is fairly stable at room temperature, the crystallization of bloedite is more likely, as discussed in a recent study.<sup>78</sup>

**Sea Salt Mixed with Soil-Derived Particles.** Sea-salt particles mixed with soil-derived particles, which were formed either by coagulation or cloud processes,<sup>18,63,72</sup> are encountered frequently due to the mixing of terrestrial and marine air masses. Nineteen particle types were identified by EPMA (see Table S1, Supporting Information). RMS analysis of these particles identified a mixture of chemical species, such as solid NaNO<sub>3</sub>, originating from reacted sea salts, together with clay minerals or calcite. A typical example is given in Figure 2. The

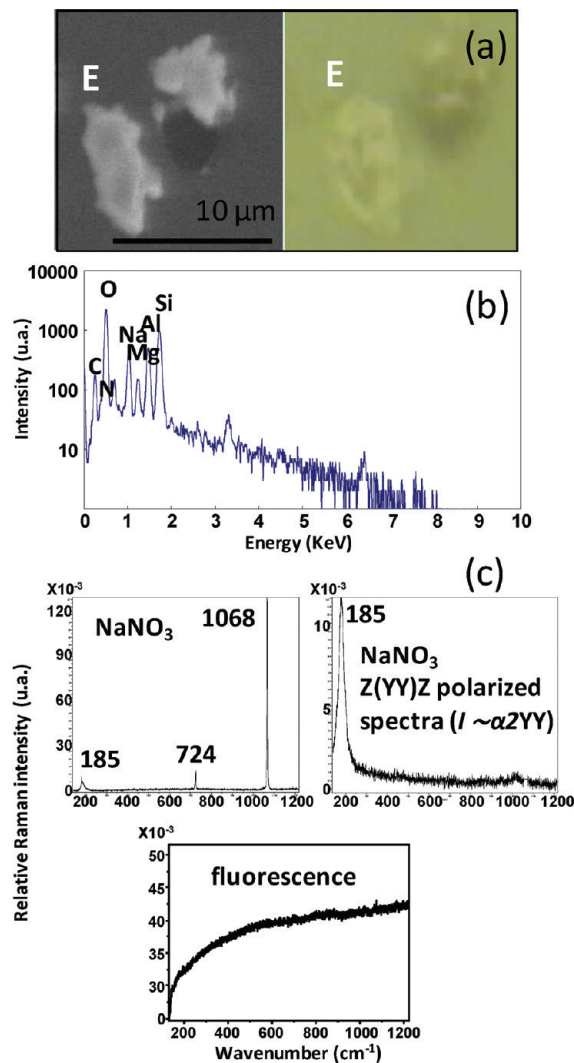


**Figure 2.** Elemental and molecular compositions of a clay mineral particle internally mixed with NaNO<sub>3</sub>: (a) SEM and optical images of particle E; (b) X-ray spectrum of particle E; (c) resolved Raman spectra of particle E.

elemental composition of particle E (Figure 2b), which was assigned to the AlSi-(Na,Mg)NO<sub>3</sub>-C particle type, was 10.0% C, 55.1% O, 1.9% N, 6.5% Na, 1.9% Mg, 7.1% Al, and 16.6% Si. RMS analysis of the same particle showed three pure spectra (Figure 2c): a NaNO<sub>3</sub> spectrum with a strong Raman band at 1068 cm<sup>-1</sup>, a NaNO<sub>3</sub> Z(YY)Z-polarized spectrum with a characteristic band at 185 cm<sup>-1</sup>, and a clay mineral spectrum

with strong fluorescence. The polarized spectrum for solid NaNO<sub>3</sub> revealed the presence of oriented NaNO<sub>3</sub> crystals within the individual particles, indicating the crystallization of NaNO<sub>3</sub> droplets before or during collection.<sup>79</sup> This type of detailed characterization of individual airborne particles highlights the potential of the combined application of these two single-particle microscopic techniques.

**Internal Mixing State of Individual Asian Dust Particles.** Among the 92 particles analyzed, 53% were internally mixed with two or more chemical species. Therefore, besides the identification of species within the individual particles, the chemical mixing of species, i.e., the distribution of molecular species within individual particles, was examined on the same particles using both elemental quantification and molecular distribution provided by EPMA and Raman imaging, respectively. Three types of internal mixing states were observed and are described as follows.

**Mixing of Nonreacted Particles.** Mixtures of nonreacted particles include particles mixed with different minerals of a soil origin and soil-derived ones mixed with genuine sea salt. Such mixing resulted mainly from particle aggregation in the atmosphere, as described for Asian dust samples.<sup>18,63,72</sup> For samples S1–S3, mixtures of soil-derived minerals accounted for 15% of the particles analyzed. Two typical examples are shown in Figure 3. The elemental composition of particle F (see Figure 3a,b), which was assigned to the (Ca,Mg)CO<sub>3</sub>-AlSi particle type by EPMA, was 24.8% C, 37.9% O, 1.4% Mg, 2.7% Al, 6.5% Si, and 26.1% Ca. The Raman spectra (Figure 3c) and images (Figure 3d) clearly indicate that particle F is an intimate mixture of two solids, such as calcite and a clay mineral within an individual particle, 2.53 μm in size, rather than two agglomerated particles. Carbonates are frequently found as a “cement” on clay minerals in soils, which can be uplifted as primary particles in the atmosphere.<sup>39</sup> Particle G in Figure 3a was assigned to the AlSi(Mg,K)-C type on the basis of its elemental composition (Figure 3b), i.e., 10.6% C, 53.0% O, 1.7% Mg, 11.4% Al, 20.0% Si, and 1.8% K. Raman imaging analysis determined particle G to be an internal mixture of a clay mineral and TiO<sub>2</sub> (anatase) (Figure 3c,d). The aluminosilicate mineral was detected using both techniques. Ti was not detected by EPMA as its content was below the detection limit, but a small amount of TiO<sub>2</sub> (<1 wt %) was detected by RMS because its Raman cross-section is high. The TiO<sub>2</sub> species is generally associated with swelling clay minerals,<sup>80</sup> and mineral dust containing minor TiO<sub>2</sub> may act as an effective photocatalyst for atmospheric chemical reactions.<sup>81,82</sup> In particular, it was recently reported that TiO<sub>2</sub> is involved in the renoxidation process.<sup>83</sup>

**Totally or Partially Reacted Particles.** A total of 33% of the analyzed particles were nitrate- and/or sulfate-containing particles, 80% of which contained nitrates, suggesting that nitrate formation is favored over sulfate formation, as previously reported.<sup>61</sup> Primary chemical species are expected to remain in the particles, such as the reacted sea-salt particle shown in Figure 4a, when the chemical reaction is incomplete. In this case, the X-ray spectra were obtained at three different locations of the particle (Figure 4b) with different concentrations of N (0–14.7%), S (1.7–6.8%), and Cl (0–17.4%). For each location, chemical species of (Na,Mg)(Cl,SO<sub>4</sub>), (Ca,Mg)SO<sub>4</sub>, or (Na,Mg)(SO<sub>4</sub>,NO<sub>3</sub>) were identified by EPMA. Three main spectra, one each for anhydrite (anhydrous CaSO<sub>4</sub>) and NaNO<sub>3</sub> and the NaNO<sub>3</sub> Z(YY)Z-polarized spectrum indicative of the crystal NaNO<sub>3</sub>, were obtained by

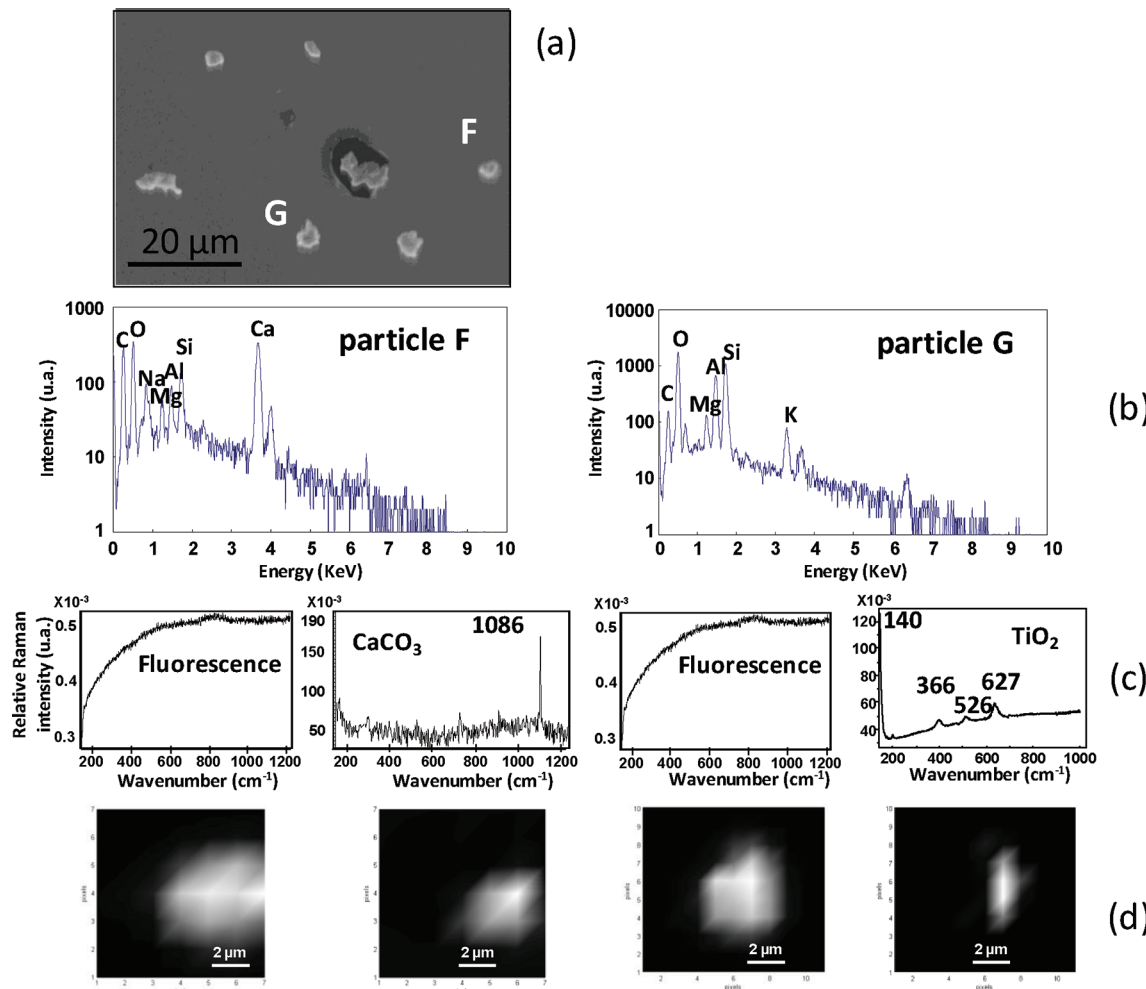


**Figure 3.** (a) SEM image, (b) X-ray spectra, (c) resolved Raman spectra, and (d) corresponding Raman images (after smoothing procedure) of the clay mineral particles internally mixed with calcite (particle F) and anatase (particle G).

Raman imaging analysis of the particle (Figure 4c), these three species being distributed heterogeneously within the particle (Figure 4d,e). Crystalline NaNO<sub>3</sub> resulted from a reaction of sea salts with nitrogen oxides, whereas anhydrous CaSO<sub>4</sub> would be formed from an atmospheric reaction between CaCO<sub>3</sub> and gaseous sulfur oxides. The reconstructed Raman images shown in Figure 4e reveal the fractionated crystallization of anhydrite and crystal NaNO<sub>3</sub>. The dark shade around the bright particle on its SEM image indicates that the particle had been collected as a water droplet and crystallization occurred on the substrate. RMS did not detect Na<sub>2</sub>SO<sub>4</sub> in the particle, but EPMA detected (Na,S)-containing species at the bottom of the aggregate (near the substrate). The depth resolution of RMS for heterogeneous, anisotropic, and mostly opaque material cannot be calculated rigorously, but was estimated to be approximately 3 μm according to the working conditions. Moreover, the laser focal point may vary inside the aggregate due to the wide range of particle thickness and be strongly dependent on the refractive index of the solid compounds probed (as explained in the Supporting Information). The laser focal point is believed to have been at the upper surface of the particle, and (Na,S)-containing species located near the substrate were not detected due to the limited penetration depth of the laser beam. Focusing the laser beam well below the particle surface was performed after the Raman mapping measurement to confirm

this hypothesis, and the obtained spectra showed the characteristic Raman bands of both NaNO<sub>3</sub> and Na<sub>2</sub>SO<sub>4</sub> species. This suggests that RMS is a surface-sensitive technique that can probe the core–shell structures by varying the working distance. Figures S3 and S4 in the Supporting Information give other examples of sea-salt particles that partially or totally reacted to form NaNO<sub>3</sub>, CaSO<sub>4</sub>·2H<sub>2</sub>O, and/or Na<sub>2</sub>Mg(SO<sub>4</sub>)<sub>2</sub>·4H<sub>2</sub>O.

Figure 5 shows the SEM image, optical image, and Raman image of a Ca-containing particle along with its X-ray and Raman spectra. According to EPMA analysis, the particle belongs to the C–Ca(SO<sub>4</sub>,CO<sub>3</sub>) particle type on the basis of its elemental concentrations, i.e., 49.6% C, 33.6% O, 9.3% Ca, and 3.5% S. Three pure Raman spectra were resolved from the RMS mapping data: those for calcium nitrate, anhydrite, and calcite. Moreover, the particle observed by optical microscopy clearly exhibited a dropletlike shape, indicating a water-soluble coating of the particle. The Raman image shows the distribution of Ca(NO<sub>3</sub>)<sub>2</sub> over the particle (Figure 5c), whereas calcite and anhydrite were observed only in a few locations in the particle (not shown). This suggests that a complete coating of CaSO<sub>4</sub> and CaCO<sub>3</sub> components by deliquescent Ca(NO<sub>3</sub>)<sub>2</sub> occurred with a core–shell structure. The molecular assignment of calcite and anhydrite species by RMS agreed with the chemical speciation by EPMA, whereas calcium nitrate was not

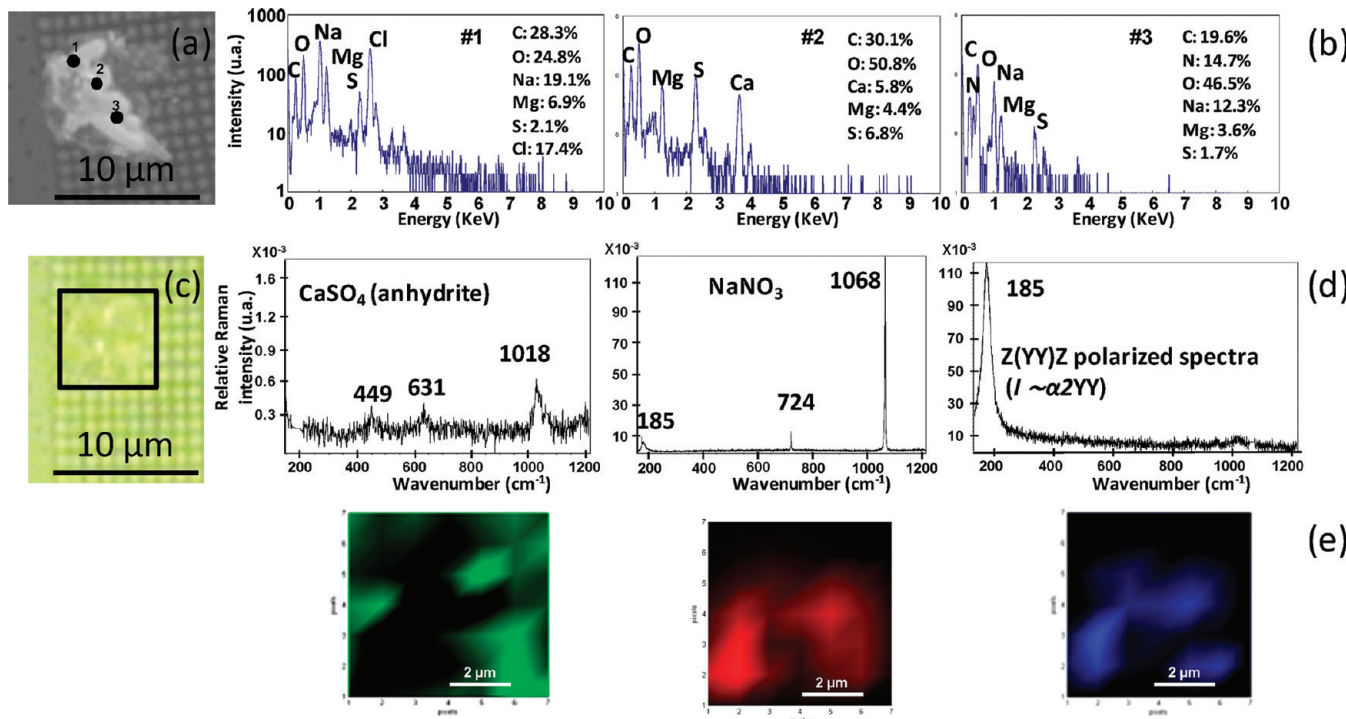


**Figure 4.** (a) SEM image of partially reacted sea-salt aggregates, (b) X-ray spectra and elemental compositions obtained at points 1, 2, and 3 (marked in (a)) of the aggregates, (c) optical image of the aggregates, (d) resolved Raman spectra of the aggregates, and (e) corresponding Raman images (after smoothing procedure) of the aggregates.

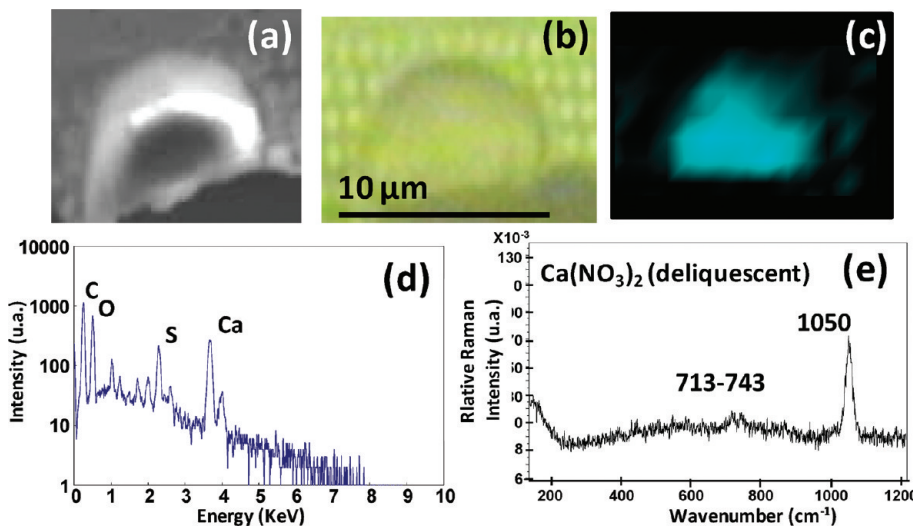


**Figure 5.** (a) SEM image, (b) optical image, (c) Raman image (after smoothing procedure), (d) X-ray spectrum, and (e) Raman spectrum of a reacted carbonate-containing particle.

expected due to the absence of a N peak in the X-ray spectrum (Figure 5d). The thin surface coating layer of deliquescent Ca(NO<sub>3</sub>)<sub>2</sub> on CaSO<sub>4</sub> and CaCO<sub>3</sub> observed by EPMA was attributed to water evaporation in the high-vacuum SEM chamber. The lack of detection of N by EPMA appeared to be due to the small sampling volume of the probing electron beam. On the other hand, the nitrate compounds were detected easily by RMS due to their high Raman cross-sections. This finding is not new, as a study using TEM/EDX also identified Asian dust particles coated with nitrates.<sup>84</sup>

**Aluminosilicate Particles Mixed with Nitrates and/or Sulfates.** Some aluminosilicate particles were observed to be

mixed with nitrates and/or sulfates (14% of the analyzed particles), which might be formed by heterogeneous reactions of gaseous nitrogen and/or sulfur oxides with nonreactive aggregated aluminosilicate particles containing reactive NaCl and/or CaCO<sub>3</sub> species. The coalescence and/or aggregation of nonreactive aluminosilicate particles with reacted particles, such as NaNO<sub>3</sub>, Na<sub>2</sub>SO<sub>4</sub>, CaSO<sub>4</sub>, and Ca(NO<sub>3</sub>)<sub>2</sub>, were also observed. Figure S5 in the Supporting Information shows the SEM image, X-ray spectrum, resolved Raman spectra, and Raman images of an aluminosilicate particle mixed with Na<sub>2</sub>SO<sub>4</sub> species, which is 3 μm in size and belongs to the AlSi–Na<sub>2</sub>SO<sub>4</sub> particle type according to EPMA. Two Raman

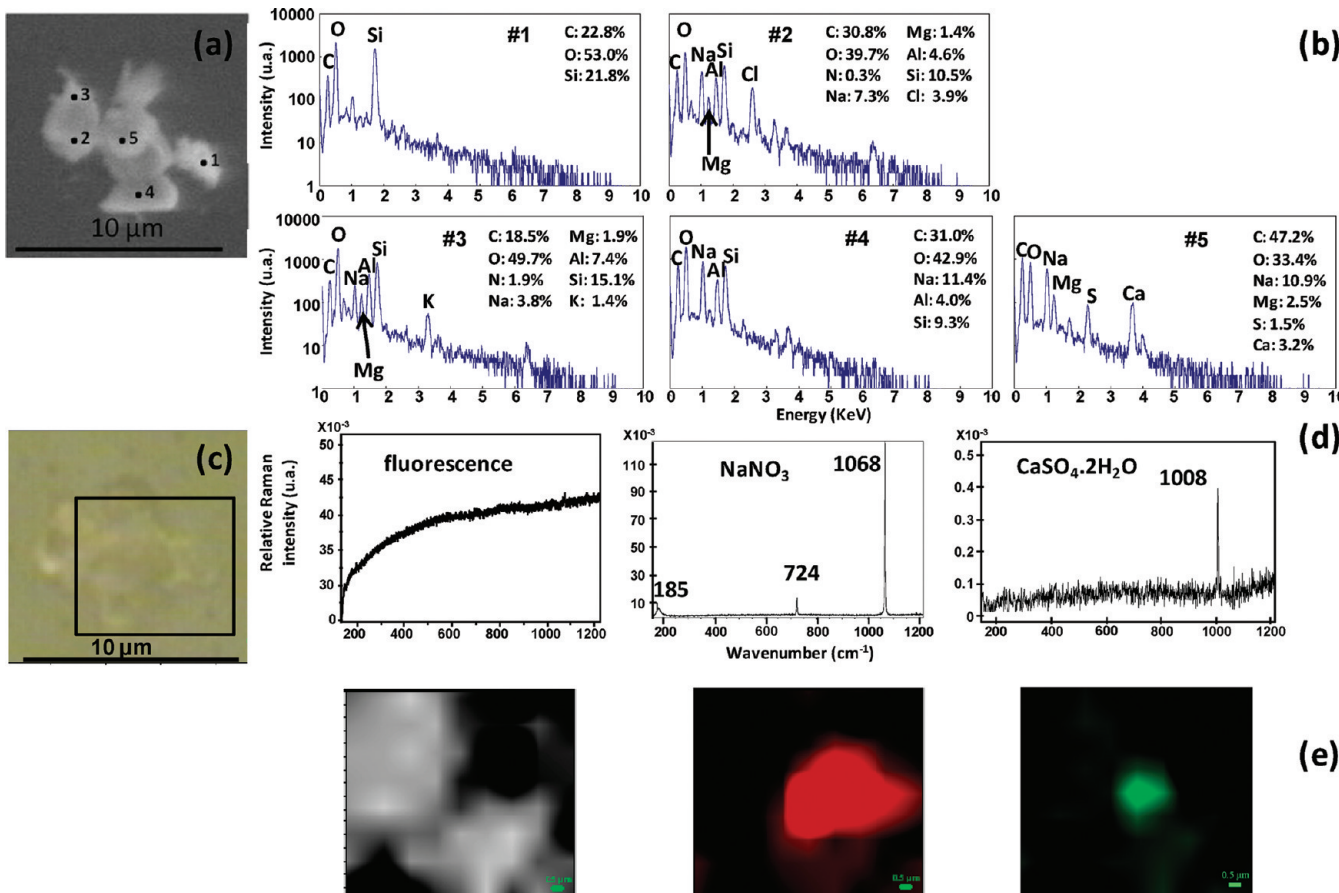


**Figure 6.** (a) SEM image, (b) X-ray spectra, (c) optical image, (d) resolved Raman spectra, and (e) corresponding Raman images (after smoothing procedure) of a nitrate-coated mineral dust aggregate.

spectra were extracted from the Raman mapping data, i.e., a fluorescent spectrum attributed to a clay mineral and a Na<sub>2</sub>SO<sub>4</sub> spectrum with its characteristic Raman band at 992 cm<sup>-1</sup>. The molecular images reconstructed for this particle (Figure S5d) clearly show an intimate mixture of the two compounds, which is likely the result of atmospheric processes rather than aggregation. Either the chemical transformation of NaCl originally aggregated on the clay mineral surface or the coalescence of deliquescent Na<sub>2</sub>SO<sub>4</sub> on the clay particle could yield its internal mixing structure. Figure S6 in the Supporting Information shows other examples of aluminosilicate particles mixed with NaNO<sub>3</sub>, for which RMS analysis identified a thin coating of NaNO<sub>3</sub> in the solid phase on the clay minerals. The mixture particles of clay mineral dust and nitrates (in the solid phase) frequently observed were attributed to the uptake of nitrate-containing particles by Asian dust during long-range transport over polluted areas.<sup>85</sup> This kind of mixing process due to nitrate formation on mineral dust particles is considered to be a sink for atmospheric NO<sub>x</sub>.

Some coarse particles were observed as aggregates, which were composed mainly of aluminosilicate minerals and nitrate species. Figure 6 shows an aggregate composed of several particles, as shown in its SEM and optical images (Figure 6a,c). From an analysis of the X-ray spectra obtained at five different locations of the aggregated particle (Figure 6b), particle types at locations 1–5 were determined to be C–SiO<sub>2</sub>, AlSi–(Na,Mg)(NO<sub>3</sub>,Cl)–C, AlSi–(Na,Mg,K)NO<sub>3</sub>–C, AlSi–C, and (Na,Mg,Ca)(CO<sub>3</sub>,SO<sub>4</sub>), respectively. RMS mapping data were obtained by scanning over the entire aggregate for which clay

minerals, oriented NaNO<sub>3</sub> crystals, and gypsum (CaSO<sub>4</sub>·2H<sub>2</sub>O) were identified as the main species (Figure 6d). Gypsum was localized in the central part of the aggregate, whereas solid NaNO<sub>3</sub> was observed to cover the entire aggregate surface, suggesting its crystallization on the aggregate surface after collection (Figure 6e). The Raman imaging results were in agreement with those from the elemental composition data obtained at the different locations in the aggregate, except at location 5, where the (Na,Mg,Ca)(CO<sub>3</sub>,SO<sub>4</sub>) type was determined by EPMA, but no carbonate was detected by RMS. For this part of the aggregate, only gypsum and sodium nitrate were identified by RMS. The carbonate species appears to have been localized at the bottom of the particle with gypsum and NaNO<sub>3</sub> distributed on the surface because the laser beam of the surface-oriented focal point mostly probed the surface. Figures S6 and S7 in the Supporting Information show examples of similar aggregates of mineral particles with a NaNO<sub>3</sub> coating. These examples demonstrate that complementary information can be obtained from the combined use of RMS and EPMA performed on the same individual particles, and particle structures can be resolved, even for complex aggregates.

## CONCLUSIONS

The composition of individual Asian dust particles was identified using both elemental and molecular analyses performed by EPMA and RMS on the same particles. Raman imaging provided clear information on the spatial distribution of species within individual particles and the spatially resolved chemical mixing state of individual particles. EPMA provided

somewhat complementary information on the chemical species of clay minerals and chloride salts for which RMS has limited chemical speciation. The suitability of the combined use of EPMA and RMS was demonstrated, where complementary physicochemical information on individual aerosol particles could be obtained by the combined use of the two single-particle analytical techniques. Studies that have used EPMA and FT-IR microimaging techniques in combination to characterize the same individual particles have been carried out by our group.<sup>35,37–39</sup> The combined use of three single-particle analytical techniques, such as EPMA, RMS, and FT-IR imaging, to characterize the same particles will be the subject of a subsequent study.

## ASSOCIATED CONTENT

### Supporting Information

Additional information as noted in text. This material is available free of charge via the Internet at <http://pubs.acs.org>.

## AUTHOR INFORMATION

### Corresponding Author

\*Phone: +82 32 860 7676. Fax: +82 32 867 5604. E-mail: curo@inha.ac.kr.

### Notes

The authors declare no competing financial interest.

## ACKNOWLEDGMENTS

This study was supported by a French–Korean joint research project funded by the CNRS (Programme Hubert Curien STAR No. 19040UJ) and by Basic Science Research Programs through the National Research Foundation of Korea (NRF) funded by the Ministry of Education, Science, and Technology (Grants 2011-0008172 and 2010-001881).

## REFERENCES

- (1) De Bock, L. A.; E., V. G. R. In *Analytical Chemistry of Aerosols*; Spurny, K. R., Ed.; Lewis Publishers: Boca Raton, FL, 1999; pp 243–272.
- (2) Deboudt, K.; Flament, P.; Choel, M.; Gloter, A.; Sobanska, S.; Colliex, C. *J. Geophys. Res. [Atmos.]* **2010**, *115*, D24207.
- (3) Fletcher, R. A.; Small, J. A.; Scott, J. H. J. In *Aerosol Measurement: Principles, Techniques, and Applications*, 2nd ed.; Baron, P. A., Willeke, K., Eds.; Wiley-Interscience: New York, 2001; pp 295–363.
- (4) Ghorai, S.; Tivanski, A. V. *Anal. Chem.* **2010**, *82*, 9289–9298.
- (5) Laskin, A. In *Fundamentals and Applications in Aerosol Spectroscopy*; Signorell, R., Reid, J., Eds.; Taylor and Francis Books, Inc.: Boca Raton, FL, 2010; pp 243–272.
- (6) Moffet, R. C.; Henn, T.; Laskin, A.; Gilles, M. K. *Anal. Chem.* **2010**, *82*, 7906–7914.
- (7) Moffet, R. C.; Tivanski, A. V.; Gilles, M. K. In *Fundamentals and Applications in Aerosol Spectroscopy*; Signorell, R., Reid, J., Eds.; Taylor and Francis Books, Inc.: Boca Raton, FL, 2010; pp 243–272.
- (8) Choel, M.; Deboudt, K.; Osán, J.; Flament, P.; Van Grieken, R. *Anal. Chem.* **2005**, *77*, 5686–5692.
- (9) Ro, C.-U.; Kim, H.; Van Grieken, R. *Anal. Chem.* **2004**, *76*, 1322–1327.
- (10) Ro, C.-U.; Osán, J.; Szalóki, I.; de Hoog, J.; Worobiec, A.; Van Grieken, R. *Anal. Chem.* **2003**, *75*, 851–859.
- (11) Ro, C.-U.; Osán, J.; Van Grieken, R. *Anal. Chem.* **1999**, *71*, 1521–1528.
- (12) Choel, M.; Deboudt, K.; Flament, P. *Water, Air, Soil Pollut.* **2010**, *209*, 93–107.
- (13) Choel, M.; Deboudt, K.; Flament, P.; Aimoz, L.; Mériaux, X. *Atmos. Environ.* **2007**, *41*, 2820–2830.
- (14) Ebert, M.; Weinbruch, S.; Hoffmann, P.; Ortner, H. M. *Atmos. Environ.* **2004**, *38*, 6531–6545.
- (15) Geng, H.; Park, Y.; Hwang, H.; Kang, S.; Ro, C.-U. *Atmos. Chem. Phys.* **2009**, *9*, 6933–6947.
- (16) Geng, H.; Ryu, J.; Jung, H.-J.; Chung, H.; Ahn, K.-H.; Ro, C.-U. *Environ. Sci. Technol.* **2010**, *44*, 2348–2353.
- (17) Kang, S.; Hwang, H.; Park, Y.; Kim, H.; Ro, C.-U. *Environ. Sci. Technol.* **2008**, *42*, 9051–9057.
- (18) Kang, S.; Hwang, H.; Park, Y.; Kim, H.; Ro, C.-U. *Atmos. Environ.* **2009**, *43*, 3445–3453.
- (19) Krueger, B. J.; Grassian, V. H.; Iedema, M. J.; Cowin, J. P.; Laskin, A. *Anal. Chem.* **2003**, *75*, 5170–5179.
- (20) Ro, C.-U.; Hwang, H.; Kim, H.; Chun, Y.; Van Grieken, R. *Environ. Sci. Technol.* **2005**, *39*, 1409–1419.
- (21) Worobiec, A.; Szalóki, I.; Osán, J.; Maenhaut, W.; Stefaniak, E. A.; Van Grieken, R. *Atmos. Environ.* **2007**, *41*, 9217–9230.
- (22) Bruns, E. A.; Perraud, V.; Zelenyuk, A.; Ezell, M. J.; Johnson, S. N.; Yu, Y.; Imre, D.; Finlayson-Pitts, B. J.; Alexander, M. L. *Environ. Sci. Technol.* **2010**, *44*, 1056–1061.
- (23) Coury, C.; Dillner, A. M. *Atmos. Environ.* **2008**, *42*, 5923–5932.
- (24) Garland, R. M.; Wise, M. E.; Beaver, M. R.; DeWitt, H. L.; Aiken, A. C.; Jimenez, J. L.; Tolbert, M. A. *Atmos. Chem. Phys.* **2005**, *5*, 1951–1961.
- (25) Gibson, E. R.; Hudson, P. K.; Grassian, V. H. *J. Phys. Chem. A* **2006**, *110*, 11785–11799.
- (26) Hoffman, R. C.; Laskin, A.; Finlayson-Pitts, B. J. *J. Aerosol Sci.* **2004**, *35*, 869–887.
- (27) Hopey, J. A.; Fuller, K. A.; Krishnaswamy, V.; Bowdle, D.; Newchurch, M. J. *Appl. Opt.* **2008**, *47*, 2266–2274.
- (28) Liu, Y.; Yang, Z.; Desyaterik, Y.; Gassman, P. L.; Wang, H.; Laskin, A. *Anal. Chem.* **2008**, *80*, 633–642.
- (29) Chan, M. N.; Chan, C. K. *Environ. Sci. Technol.* **2003**, *37*, 5109–5115.
- (30) Freedman, M. A.; Baustian, K. J.; Wise, M. E.; Tolbert, M. A. *Anal. Chem.* **2010**, *82*, 7965–7972.
- (31) Treuel, L.; Sandmann, A.; Zellner, R. *ChemPhysChem* **2011**, *12*, 1109–1117.
- (32) Batonneau, Y.; Brémard, C.; Gengembre, L.; Laureyns, J.; Le Maguer, A.; Le Maguer, D.; Perdris, E.; Sobanska, S. *Environ. Sci. Technol.* **2004**, *38*, 5281–5289.
- (33) Batonneau, Y.; Sobanska, S.; Laureyns, J.; Brémard, C. *Environ. Sci. Technol.* **2006**, *40*, 1300–1306.
- (34) Nelson, M. P.; Zugates, C. T.; Treado, P. J.; Casuccio, G. S.; Exline, D. L.; Schlaegle, S. F. *Aerosol Sci. Technol.* **2001**, *34*, 108–117.
- (35) Ryu, J.; Ro, C.-U. *Anal. Chem.* **2009**, *81*, 6695–6707.
- (36) Sobanska, S.; Falgayrac, G.; Laureyns, J.; Brémard, C. *Spectrochim. Acta, Part A* **2006**, *64*, 1102–1109.
- (37) Jung, H.-J.; Malek, M. A.; Ryu, J.; Kim, B.; Song, Y.-C.; Kim, H.; Ro, C.-U. *Anal. Chem.* **2010**, *82*, 6193–6202.
- (38) Song, Y.-C.; Ryu, J.; Malek, M. A.; Jung, H.-J.; Ro, C.-U. *Anal. Chem.* **2010**, *82*, 7987–7998.
- (39) Malek, M. A.; Kim, B.; Jung, H.-J.; Song, Y.-C.; Ro, C.-U. *Anal. Chem.* **2011**, *83*, 7970–7977.
- (40) Stefaniak, E. A.; Buczynska, A.; Novakovic, V.; Kuduk, R.; Van Grieken, R. In *Second International Workshop on Non-Equilibrium Processes in Plasmas and Environmental Science*; Petrovic, Z. L., Malovic, G., Maric, D., Eds.; IOP Publishing Ltd.: Bristol, U.K., 2009; Vol. 162.
- (41) Stefaniak, E. A.; Worobiec, A.; Potgieter-Vermaak, S.; Alseczc, A.; Török, S.; Van Grieken, R. *Spectrochim. Acta, Part B* **2006**, *61*, 824–830.
- (42) Worobiec, A.; Potgieter-Vermaak, S.; Brooker, A.; Darchuk, L.; Stefaniak, E.; Van Grieken, R. *Microchem. J.* **2010**, *94*, 65–72.
- (43) *Climate Change 2007: The Physical Science Basis. Contribution of Working Group I to the Fourth Assessment*; Report of the Intergovernmental Panel on Climate Change; Cambridge, U.K., 2007.
- (44) Uno, I.; Eguchi, K.; Yumimoto, K.; Takemura, T.; Shimizu, A.; Uematsu, M.; Liu, Z. Y.; Wang, Z. F.; Hara, Y.; Sugimoto, N. *Nat. Geosci.* **2009**, *2*, 557–560.

- (45) Wang, K. C.; Dickinson, R. E.; Liang, S. L. *Science* **2009**, *323*, 1468–1470.
- (46) Bergstrom, R. W.; Pilewskie, P.; Russell, P. B.; Redemann, J.; Bond, T. C.; Quinn, P. K.; Sierau, B. *Atmos. Chem. Phys.* **2007**, *7*, 5937–5943.
- (47) Andreae, M. O.; Rosenfeld, D. *Earth-Sci. Rev.* **2008**, *89*, 13–41.
- (48) Manktelow, P. T.; Carslaw, K. S.; Mann, G. W.; Spracklen, D. V. *Atmos. Chem. Phys.* **2010**, *10*, 365–382.
- (49) Baker, A. R.; Kelly, S. D.; Biswas, K. F.; Witt, M.; Jickells, T. D. *Geophys. Res. Lett.* **2003**, *30*, 2296.
- (50) Paytan, A.; Mackey, K. R. M.; Chen, Y.; Lima, I. D.; Doney, S. C.; Mahowald, N.; Labiosa, R.; Postf, A. F. *Proc. Natl. Acad. Sci. U. S. A.* **2009**, *106*, 4601–4605.
- (51) Price, H. U.; Jaffe, D. A.; Cooper, O. R.; Doskey, P. V. *J. Geophys. Res., [Atmos.]* **2004**, *109*, D23S13.
- (52) Sullivan, R. C.; Guazzotti, S. A.; Sodeman, D. A.; Prather, K. A. *Atmos. Chem. Phys.* **2007**, *7*, 1213–1236.
- (53) Li-Jones, X.; Maring, H. B.; Prospero, J. M. *J. Geophys. Res., [Atmos.]* **1998**, *103*, 31113–31121.
- (54) Xu, J.; Bergin, M. H.; Greenwald, R.; Schauer, J. J.; Shafer, M. M.; Jaffrezo, J. L.; Aymoz, G. *J. Geophys. Res., [Atmos.]* **2004**, *109*, D19S03.
- (55) Arimoto, R.; Zhang, X. Y.; Huebert, B. J.; Kang, C. H.; Savoie, D. L.; Prospero, J. M.; Sage, S. K.; Schloesslin, C. A.; Khaing, H. M.; Oh, S. N. *J. Geophys. Res., [Atmos.]* **2004**, *109*, D19S04.
- (56) Cohen, D. D.; Garton, D.; Stelcer, E.; Hawas, O.; Wang, T.; Poon, S.; Kim, J.; Choi, B. C.; Oh, S. N.; Shin, H. J.; Ko, M. Y.; Uematsu, M. *J. Geophys. Res., [Atmos.]* **2004**, *109*, D19S12.
- (57) Huebert, B. J.; Bates, T.; Russell, P. B.; Shi, G. Y.; Kim, Y. J.; Kawamura, K.; Carmichael, G.; Nakajima, T. *J. Geophys. Res., [Atmos.]* **2003**, *108*, 8633.
- (58) Maxwell-Meier, K.; Weber, R.; Song, C.; Orsini, D.; Ma, Y.; Carmichael, G. R.; Streets, D. G. *J. Geophys. Res., [Atmos.]* **2004**, *109*, D19S07.
- (59) McNaughton, C. S.; Clarke, A. D.; Howell, S. G.; Moore, K. G.; Brekhovskikh, V.; Weber, R. J.; Orsini, D. A.; Covert, D. S.; Buzorius, G.; Brechtel, F. J.; Carmichael, G. R.; Tang, Y. H.; Eisele, F. L.; Mauldin, R. L.; Bandy, A. R.; Thornton, D. C.; Blomquist, B. J. *Geophys. Res., [Atmos.]* **2004**, *109*, D19S06.
- (60) Geng, H.; Ryu, J.; Maskey, S.; Jung, H.-J.; Ro, C.-U. *Atmos. Chem. Phys.* **2011**, *11*, 1327–1337.
- (61) Hwang, H.; Kim, H.; Ro, C.-U. *Atmos. Environ.* **2008**, *42*, 8738–8746.
- (62) Kim, Y. J.; Woo, J.-H.; Ma, Y.-I.; Kim, S.; Nam, J. S.; Sung, H.; Choi, K.-C.; Seo, J.; Kim, J. S.; Kang, C.-H.; Lee, G.; Ro, C.-U.; Chang, D.; Sunwoo, Y. *Atmos. Environ.* **2009**, *43*, 5556–5566.
- (63) Ro, C.-U.; Oh, K.-Y.; Kim, H.; Kim, Y. P.; Lee, C. B.; Kim, K.-H.; Kang, C. H.; Osán, J.; de Hoog, J.; Worobiec, A.; Van Grieken, R. *Environ. Sci. Technol.* **2001**, *35*, 4487–4494.
- (64) Godoi, R. H. M.; Potgieter-Vermaak, S.; De Hoog, J.; Kaegi, R.; Van Grieken, R. *Spectrochim. Acta, Part A* **2006**, *61*, 375–388.
- (65) Maskey, S.; Choel, M.; Kang, S.; Hwang, H.; Kim, H.; Ro, C.-U. *Anal. Chim. Acta* **2010**, *658*, 120–127.
- (66) Sadezky, A.; Muckenhuber, H.; Grothe, H.; Niessner, R.; Pöschl, U. *Carbon* **2005**, *43*, 1731–1742.
- (67) Windig, W.; Antalek, B.; Lippert, J. L.; Batonneau, Y.; Brémard, C. *Anal. Chem.* **2002**, *74*, 1371–1379.
- (68) Vekemans, B.; Janssens, K.; Vincze, L.; Adams, F.; Van Espen, P. *X-Ray Spectrom.* **1994**, *23*, 278–285.
- (69) Choël, M.; Deboudt, K.; Flament, P. *Microsc. Res. Tech.* **2007**, *70*, 996–1002.
- (70) Park, S. S.; Kim, Y. J.; Cho, S. Y.; Kim, S. J. *J. Air Waste Manage. Assoc.* **2007**, *57*, 434–443.
- (71) Herman, R. G.; Bogdan, C. E.; Sommer, A. J.; Simpson, D. R. *Appl. Spectrosc.* **1987**, *41*, 437–440.
- (72) Hwang, H.; Ro, C.-U. *J. Geophys. Res., [Atmos.]* **2005**, *110*, D23201.
- (73) Hwang, H.; Ro, C.-U. *Spectrochim. Acta* **2006**, *B61*, 400–406.
- (74) Hwang, H.; Ro, C.-U. *Atmos. Environ.* **2006**, *40*, 3869–3880.
- (75) Tobe, Y.; Zhang, D.; Matsuki, A.; Iwasaka, Y. *Proc. Natl. Acad. Sci. U.S.A.* **2010**, *107*, 17905–17910.
- (76) Takahashi, Y.; Miyoshi, T.; Yabuki, S.; Inada, Y.; Shimizu, H. *Atmos. Environ.* **2008**, *42*, 6535–6541.
- (77) Liu, Y. J.; Zhu, T.; Zhao, D. F.; Zhang, Z. F. *Atmos. Chem. Phys.* **2008**, *8*, 7205–7215.
- (78) Vargas Jentzsch, P.; Kampe, B.; Röscher, P.; Popp, J. r. *J. Phys. Chem. A* **2011**, *115*, 5540–5546.
- (79) Scolaro, S.; Sobanska, S.; Barbillat, J.; Laureyns, J.; Louis, F.; Petitprez, D.; Brémard, C. *J. Raman Spectrosc.* **2009**, *40*, 157–163.
- (80) Allo, W. *Clays Clay Miner.* **2004**, *52*, 304–310.
- (81) Monge, M. E.; D'Anna, B.; George, C. *Phys. Chem. Chem. Phys.* **2010**, *12*, 8991–8998.
- (82) Ndour, M.; D'Anna, B.; George, C.; Ka, O.; Balkanski, Y.; Kleffmann, J.; Stemmler, K.; Ammann, M. *Geophys. Res. Lett.* **2008**, *35*, L05812.
- (83) Ndour, M.; Conchon, P.; D'Anna, B.; Ka, O.; George, C. *Geophys. Res. Lett.* **2009**, *36*, L05816.
- (84) Li, W. J.; Shao, L. Y. *Atmos. Chem. Phys.* **2009**, *9*, 1863–1871.
- (85) Matsuki, A.; Iwasaka, Y.; Shi, G.; Zhang, D.; Trochkine, D.; Yamada, M.; Kim, Y.-S.; Chen, B.; Nagatani, T.; Miyazawa, T.; Nagatani, M.; Nakata, H. *Geophys. Res. Lett.* **2005**, *32*, L22806.